This is the Accepted Manuscript version of an article accepted for publication in Journal of Applied Physics. The Version of Record is available online at http://dx.doi.org/10.1063/1.4995368.

Detailed numerical simulation of cathode spots in vacuum arcs: interplay of different mechanisms and ejection of droplets

H. T. C. Kaufmann[1,2], M. D. Cunha[1,2], M. S. Benilov[1,2], W. Hartmann[3], and N. Wenzel[3]

[1]Departamento de Física, Faculdade de Ciências Exatas e da Engenharia, Universidade da Madeira, Largo do Município, 9000 Funchal, Portugal

[2]Instituto de Plasmas e Fusão Nuclear, Instituto Superior Técnico, Universidade de Lisboa, 1041 Lisboa, Portugal

[3]Siemens AG, Corporate Technology, Günther-Scharowsky-Strasse 1, 91058 Erlangen, Germany

Abstract

A model of cathode spots in high-current vacuum arcs is developed with account of all the potentially relevant mechanisms: the bombardment of the cathode surface by ions coming from a pre-existing plasma cloud; vaporization of the cathode material in the spot, its ionization and the interaction of the produced plasma with the cathode; the Joule heat generation in the cathode body; melting of the cathode material and motion of the melt under the effect of the plasma pressure and the Lorentz force and related phenomena. After the spot has been ignited by the action of the cloud (which takes a few nanoseconds), the metal in the spot is melted and accelerated toward the periphery of the spot, the main driving force being the pressure due to incident ions. Electron emission cooling and convective heat transfer are dominant mechanisms of cooling in the spot, limiting the maximum temperature of the cathode to approximately $4700 - 4800\,\mathrm{K}$. A crater is formed on the cathode surface in this way. After the plasma cloud has been extinguished, a liquid-metal jet is formed and a droplet is ejected. No explosions have been observed. The modeling results conform to estimates of different mechanisms of cathode erosion derived from the experimental data on the net and ion erosion of copper cathodes.

Keywords: Vacuum arcs, Electrodes, Arc discharges.

1 Introduction

Cathode attachments in vacuum arcs are non-stationary and consist of a number of short-lived spots. The most commonly accepted understanding of the life cycle of an individual spot is as follows; e.g., [1–3] and references therein. Micrometer-scale nonuniformities, e.g., microprotrusions, are characteristic of cathode surfaces. It is assumed that a plasma cloud (a plasma generated at the arc triggering or a plasma left over from a previous spot in the immediate vicinity) is present in the vicinity of such a microprotrusion. The ion current from the cloud heats the cathode surface, thus igniting a spot. The microprotrusion is rapidly overheated through Joule heating and explodes, with the resulting metal vapor expanding in all directions. This metal vapor is ionized and, in turn, starts heating a nearby protrusion *etc.*

The above physical picture represents one of the scenarios leading to the formation of explosive emission centers, or ectons [3]. It was suggested a long time ago, but still remains a hypothesis; experimental observations and measurements cannot provide an unambiguous verification. In such a situation, it is natural to attempt a validation of this hypothesis by means of a self-consistent numerical modeling of an individual cathode spot in a vacuum arc.

This task is hindered by the diverse and complex nature of mechanisms dominating the physics of cathode spots: the bombardment of the cathode surface by ions coming from the leftover plasma cloud; vaporization of the cathode material in the spot, its subsequent ionization and the interaction of the produced plasma with the cathode; Joule heating in the cathode body; melting of the cathode and motion of the molten metal under the effect of the plasma pressure and the Lorentz force. There seem to be no papers in which all these effects have been taken into account.

The most complete modeling of a cathode spot in a vacuum arc up to now is given in works [4–7]. In [4], the hydrodynamic aspects are considered in a simplified way, on the basis of analysis of the pressure balance at the plasma-cathode interface. In [5, 6], the hydrodynamic aspects were treated in a more accurate way, on the basis of the Navier-Stokes equations. However, no mechanism of current transfer to the cathode surface was considered in [5] and only the ion current from the plasma cloud was accounted for in [6].

In [7], the thermal development of the spot under the effect of all the above mechanisms except the motion of the molten metal was studied. Several phases of life of an individual cathode spot have been identified: the ignition, the expansion over the cathode surface, and the thermal runaway (microexplosion) or destruction of the spot by heat removal into the bulk of the cathode due to thermal conduction. It was shown that electron emission significantly affects the development of the spot, in particular, limiting the cathode surface temperature during the expansion phase and preventing thermal runaway development until the Joule heating becomes appreciable.

The aim of this paper is to study the ignition and development of cathode spots of vacuum arcs with account of all the above mechanisms. To this end, the model [7] is supplemented with an account of the motion of the molten metal and related phenomena: deformation of the molten surface, surface tension effects, and convective heat transfer. Several features of the development of the cathode spot reported in [7] remain present in the framework of the more detailed physical picture given here: the ignition and expan-

sion phases remain clearly identifiable; the plateau in the maximum cathode temperature evolution during the expansion phase remains present; the destruction of the spot by heat removal into the bulk of the cathode due to thermal conduction (accompanied by solidification of the molten metal) occurs after the leftover plasma cloud has been extinguished. The motion of the molten metal comes into play on a time scale longer than the spot ignition times, which is why the results [7] on the spot ignition time and the initial stage of the expansion phase remain applicable. On the other hand, no thermal explosion occurs: the development of the spot results in the formation of a crater and a molten metal jet, and the ejection of a droplet.

The outline of the paper is as follows. The numerical model is introduced in Sec. 2. Results of simulation are reported and discussed in Sec. 3. Conclusions are summarized in Sec. 4.

2 The model

2.1 Equations and boundary conditions

The model comprises the time-dependent heat conduction equation, describing heat transfer in the cathode body (including both the melt and the solid part); the equation of current continuity in the cathode body, supplemented with Ohm's law; and the continuity and Navier-Stokes equations, written in the incompressible form and describing the motion of the melt:

$$\rho c_p \frac{\partial T}{\partial t} + \rho c_p \mathbf{u} \cdot \nabla T = \nabla \cdot (\kappa \nabla T) + \sigma (\nabla \varphi)^2, \tag{1}$$

$$\nabla \cdot \mathbf{j} = 0, \tag{2}$$

$$\nabla \cdot \mathbf{u} = 0, \tag{3}$$

$$\rho \frac{\partial \mathbf{u}}{\partial t} + \rho (\mathbf{u} \cdot \nabla) \mathbf{u} = \nabla \cdot \left[-p\mathbf{I} + \mu (\nabla \mathbf{u} + (\nabla \mathbf{u})^T) \right] + \mathbf{j} \times \mathbf{B}. \tag{4}$$

Here ρ is the the mass density of the metal, c_p, κ, σ and μ are, respectively, the specific heat, the thermal and electrical conductivities of the metal, and the viscosity of the melt (known functions of the temperature T), φ is the electric potential, $\mathbf{u}$ is the velocity, p is the pressure, $\mathbf{I}$ is the identity tensor, $\mathbf{j} = -\sigma \nabla \varphi$ is the density of electric current in the cathode body, and $\mathbf{B}$ is the magnetic field. The second term on the lhs of Eq. (1) describes the convective heat transfer in the molten part of the cathode (an effect not taken into account in the model [7]); in the solid part this term vanishes. The last term on the rhs of Eq. (4) represents the Lorentz force.

The equations are solved under the assumption of axial symmetry in cylindrical coordinates (r, z). Only self-induced magnetic field is taken into account, so $\mathbf{B}$ has only the azimuthal component which is related to the axial component of the current density $\mathbf{j}$ in the cathode body by Ampère's law. The calculation domain for Eqs. (1) and (2) is the whole of the cathode, including both the melt and the solid part. The boundary conditions for these equations are the same as in [7]. In particular, the boundary conditions

on the cathode surface are

$$\kappa \mathbf{n} \cdot \nabla T = q_1 + q_2, \qquad \sigma \mathbf{n} \cdot \nabla \varphi = j_1 + j_2, \tag{5}$$

where $\mathbf{n}$ is the unit vector normal to the cathode surface and directed outward, q_1 and j_1 are contributions to the densities of energy flux and electric current from the plasma to the cathode surface due to the vapor emitted in the spot, ions and electrons produced by ionization of the vapor, and the electron emission from the cathode surface, and q_2 and j_2 are densities of energy flux and electric current transported by the ions from the leftover plasma cloud; see below.

The calculation domain for Eqs. (3) and (4) is the molten part of the cathode. The boundary condition at the cathode surface is

$$\left[-p\mathbf{I} + \mu(\nabla \mathbf{u} + (\nabla \mathbf{u})^T)\right] \cdot \mathbf{n} = -p_{pl}\mathbf{n} + \mathbf{F}_{st}, \tag{6}$$

where p_{pl} is the pressure exerted over the cathode surface by the plasma (see Sec. 2.2 below) and $\mathbf{F}_{st}$ is the surface tension force evaluated in the usual way in terms of the curvature of the molten cathode surface and the surface tension coefficient of the cathode material. The velocity $\mathbf{u}$ vanishes at the interface between the molten and solid metal.

The problem is solved numerically by means of the commercial software COMSOL Multiphysics. The enthalpy-porosity method [8, 9] is used for modeling the solid-liquid phase transition in the cathode body. The account of the latent heat of melting is introduced along the same lines as is done in simulation of metal casting [10]. The level-set method [11, 12] is implemented for tracking the deformation of the molten cathode surface on a fixed grid. Surface tension effects are handled within the framework of the level-set method through the continuous surface force model [13].

Note that a similar physical problem for plasma-anode interaction in vacuum arcs has been solved in works [14–17] by means of the software FLUENT. The enthalpy-porosity method was used for the modeling of the solid-liquid phase transition in the anode body, although the approach differs from the one used in this work: the energy conservation equation is solved in terms of the enthalpy instead of the temperature. In [17], the anode surface deformation is simulated by means of the volume-of-fluid method, which is an alternative to the level-set method used in this work.

COMSOL Multiphysics offers the option of modeling compressible ($\rho = \rho(p, T)$), weakly compressible ($\rho = \rho(T)$), or incompressible flows ($\rho = const$). It follows from the analysis in Appendix A that the most accurate formulation for the continuity and Navier-Stokes equations in the modeling of this work would be the weakly compressible one. However, an attempt to use the weakly compressible form, which is supposedly compatible with the level-set method used to track the deformation of the molten surface, proved unsuccessful. Such an issue requires further extensive investigation, which was not carried out in this work. Instead, the incompressible formulation of the continuity and Navier-Stokes equations is used (Eqs. (3) and (4)); the temperature dependence of the mass density described in Appendix A is used in the heat and Navier-Stokes equations, without account of the temporal and spatial derivatives of ρ in the continuity equation.

In order to validate the hydrodynamics part of the model, a simplified version was built similar to the model [5]: the account of current transfer to the cathode was discarded,

the contributions of the plasma produced in the spot were neglected. The simulation reproduces results of [5] with only minor discrepancies, which can be attributed to differences in the chosen temperature dependencies of the material properties of copper and the distinct numerical methods employed.

Simulation results reported in this paper refer to cathodes made of copper, with a Gaussian-shaped microprotrusion as in [7] and planar. The (temperature-dependent) mass density, specific heat, and thermal and electrical conductivities of copper are specified as in [7]. Data on the temperature-dependent viscosity and the temperature-dependent surface tension coefficient of liquid copper are taken from the experimental works [18] and [19], respectively.

Quantities q_1, q_2, j_1, and j_2 in Eq. (5) are evaluated in the same way as in [7]. In particular, q_1 and j_1 are obtained by means of the model of near-cathode plasma layers in vacuum arcs [20], based on a numerical simulation of the near-cathode space-charge sheath with ionization of atoms vaporized from the cathode surface [21]. (Note that the flux of vaporized atoms is evaluated in the model [20] by means of the Langmuir formula and the electron emission current is evaluated by means of the Murphy and Good formalism [22].) The contributions of the ions from the leftover plasma cloud to the energy flux and current from the plasma to the cathode surface are written as

$$q_2 = q_i^{(\mathrm{cl})}\, f_1\,(r)\;\, f_2\,(t)\,, \qquad j_2 = j_i^{(\mathrm{cl})}\, f_1\,(r)\;\, f_2\,(t)\,. \tag{7}$$

Here $q_i^{(\mathrm{cl})} = 1.1 \times 10^{12}\,\mathrm{W/\,m^2}$; $j_i^{(\mathrm{cl})} = 5.6 \times 10^{10}\,\mathrm{A/\,m^2}$; and $f_1\,(r)$ and $f_2\,(t)$ are functions characterizing the spatial distribution and temporal variation of the leftover plasma cloud and assumed in the form

$$f_1(r) = \exp\left[-\left(\frac{r}{a}\right)^2\right], \quad f_2\,(t) = \begin{cases} 1, & t \leqslant \tau \\ \exp\left(-\left(\frac{t-\tau}{\tau_0}\right)^2\right), & t > \tau \end{cases}, \tag{8}$$

where a, τ, and τ_0 are given parameters.

Note that parameters $q_i^{(\mathrm{cl})}$ and $j_i^{(\mathrm{cl})}$ (the maximum densities of energy flux and electric current transported by the ions from the leftover plasma cloud to the cathode surface) may be expressed in terms of the maximum ion density n_i, electron temperature T_e, and average charge state Z in the plasma cloud:

$$q_i^{(\mathrm{cl})} = j_i^{(\mathrm{cl})}\left(U + \frac{A}{e}\right), \qquad j_i^{(\mathrm{cl})} = Zen_i\sqrt{\frac{kZT_e}{m_i}}, \tag{9}$$

where e is the electron charge, m_i is the ion mass, k is the Boltzmann constant, and the term A describes the energy with which an ion enters the sheath and the energy released at the surface due to neutralization of an ion and condensation. In the simplest case $Z = 1$, $A = kT_e/2 + A_i - A_f + A_v$, where A_i is the ionization energy, A_f is the work function, and A_v is the vaporization energy per atom.

Values of n_i and T_e reported in the literature vary over a wide range (e.g., [1, 2] and references therein): values of n_i higher than $10^{28}\,\mathrm{m^{-3}}$ have been estimated for distances less than $1\,\mu$m from the cathode surface and values in the range $(3-6)\times10^{26}\,\mathrm{m^{-3}}$ has been estimated for up to $5\,\mu$m from the surface; reported values of the electron temperature

near the spot vary from 2 eV up to $4-6$ eV. The average charge state in a vacuum arc discharge with copper electrodes has been measured as $Z \approx 2$ (e.g., [23, 24]), but the measurements have been performed in the anodic region of the arc, i.e., far away from the region of interest for this work, which is a few microns from the cathode surface. In this work, the values $n_i = 2 \times 10^{26}\,\mathrm{m}^{-3}$, $T_e = 2\,\mathrm{eV}$, and $Z = 1$ have been assumed. The term A/e in the parentheses on the rhs of the first equation (9) is around 7.4 V, which is small compared to U, and is neglected. This gives the above-mentioned values $q_i^{(\mathrm{cl})} = 1.1 \times 10^{12}\,\mathrm{W/m^2}$ and $j_i^{(\mathrm{cl})} = 5.6 \times 10^{10}\,\mathrm{A/m^2}$.

The near-cathode voltage drop U is set equal to 20 V, which corresponds to initiation of spots under conditions of high-current vacuum arcs typical, e.g., for high-power circuit breakers. The parameters τ and a in Eq. (8) were set equal to 25 ns and 5 μm, respectively, unless indicated otherwise. (These values have been chosen on the basis of experimental data on the lifetime of an individual spot on copper cathodes [25–27], and on the spatial extension of the plasma cloud produced by a spot [2, 28]. The effect of the variation of these parameters on the spot ignition was studied in [7].) The characteristic time τ_0 was set equal to 1 ns.

2.2 Plasma pressure acting on the cathode surface

The plasma pressure p_{pl} acting on the cathode surface comprises contributions of the plasma produced from the metal vapor emitted in the spot and of the leftover plasma cloud, evaluated independently of each other: $p_{pl} = p_1 + p_2$. As in [7], this simple superposition neglects a nonlinear interaction between the leftover plasma and the freshly-produced vapor from the spot.

The contribution $p_1 = p_1(T_w, U)$ is computed as a function of the local cathode surface temperature T_w and the near-cathode voltage drop U by means of the model of near-cathode space-charge sheaths in vacuum arcs [21], based on a self-consistent description of ionization of evaporated atoms in the sheath and of a maximum of potential occurring inside the sheath. The sheath thickness is much smaller than the scale of ion-atom collisions (cf. Fig. 7b of [7]), hence the total energy of an ion is conserved. The velocity of ions generated at a point z when they have reached a point x will be (designations used in this section are the same as those in [21])

$$v_i(x,z) = \pm\sqrt{\frac{2e}{m_i}\left[\varphi(z) - \varphi(x)\right]}. \tag{10}$$

The ions generated in the region $x < 0$ (i.e., between the cathode and the point of the maximum of potential) move back to the cathode. The ions generated in the region $x > 0$ move into the plasma. We are interested in the ions moving back to the cathode, hence Eq. (10) should be applied for $x < z < 0$ with the sign minus.

The number of ions generated in the layer $z \le x \le z + dz$ per unit time and unit area (i.e., the density of ion flux generated in this layer) is $w(z)\,dz$. When these ions have reached a point x positioned between the point z and the cathode, their speed is $|v_i(x,z)|$ and the density of flux of momentum transported by these ions in the direction to the cathode is $-w(z)\,dz\,m_i v_i(x,z)$. The total density of flux of momentum of ions in the

direction to the cathode at a point x is

$$p_1(x) = -m_i \int_x^0 w(z)\, v_i(x,z)\, dz. \tag{11}$$

Eq. (14) of [21] in dimensional variables reads

$$\frac{\varepsilon_0}{2n_e^{(0)}kT_e}\left(\frac{d\varphi}{dx}\right)^2 = e^{\Phi} - 1 - \frac{\sqrt{2m_i e}k_i}{n_e^{(0)}kT_e}\int_0^x n_e(z)\, n_a(z)\sqrt{\varphi(z)-\varphi(x)}\, dz. \tag{12}$$

Taking into account Eqs. (10), (11) and the equality $w = k_i n_e n_a$, Eq. (12) may be rewritten as

$$p_1(x) = \frac{\varepsilon_0}{2}\left(\frac{d\varphi}{dx}\right)^2 + n_e^{(0)}kT_e\left(1-e^{\Phi}\right). \tag{13}$$

Here $\Phi = \frac{e\varphi}{kT_e} - \frac{e\varphi^{(0)}}{kT_e}$ as in [21]. Thus, the ion pressure is expressed in terms of the local electric field and potential and of parameters at the point of maximum of potential (values of potential $\varphi^{(0)}$ and electron density $n_e^{(0)}$). Since all the ions are absorbed by the cathode surface in the framework of the model considered, the pressure exerted on the cathode by the ions equals the flux of momentum of the incident ions and may be evaluated by means of Eq. (13) applied at the cathode surface.

Note that Eq. (13) has a clear physical meaning, which is revealed by rewriting this equation in the form

$$p_1(x) + n_e kT_e - n_e^{(0)}kT_e = \frac{\varepsilon_0}{2}\left(\frac{d\varphi}{dx}\right)^2. \tag{14}$$

The lhs of this equation represents the pressure difference to which the plasma layer between the point x and the potential maximum is subjected, while the rhs represents the integral (electrostatic) force acting on this layer, evaluated with the use of the Poisson equation.

Expression (13) at the cathode surface is evaluated by means of the same Fortran code which is used for evaluation of q_1 and j_1; the term e^{Φ} in Eq. (13) is exponentially small at the cathode surface and is neglected.

The contribution of the leftover plasma cloud is written as

$$p_2 = p_i^{(\mathrm{cl})} f_1(r)\, f_2(t), \quad p_i^{(\mathrm{cl})} = \frac{2\, q_i^{(\mathrm{cl})}}{\sqrt{2eU/m_i}}.$$

Note that the quantity $\sqrt{2eU/m_i}$ has the meaning of speed of the ions impinging on the cathode surface estimated neglecting the kinetic energy of the ions at the sheath edge.

As an example, the data on p_1 in the range of temperatures relevant to the simulations of this work and the value of $p_i^{(\mathrm{cl})}$ are shown in Fig. 1. One can see that $p_i^{(\mathrm{cl})}$ exceeds p_1 by at least a factor of 2; however, p_1 is important and should not be neglected as shown below.

Also shown in Fig. 1 is the saturated vapor pressure p_v. One can see that p_v is significantly smaller than p_1 and $p_i^{(\mathrm{cl})}$. Furthermore, p_v is significantly smaller than the

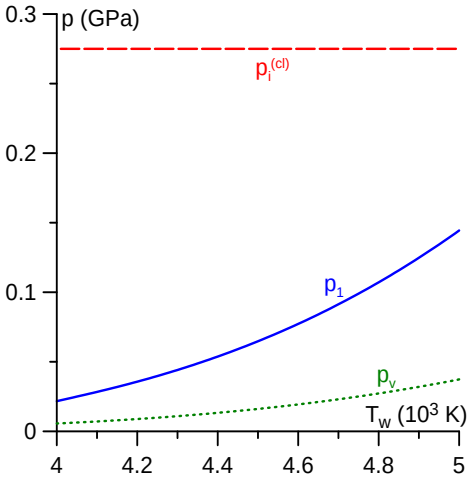

Figure 1. p_1: the pressure exerted by incident ions produced by the ionization of the metal vapor emitted in the spot as function of the cathode surface temperature T_w. $p_i^{(cl)}$: pressure due to incident ions originating from the leftover plasma cloud. p_v: saturated vapor pressure.

pressure inside the metal, which is close to $p_{pl} = p_1 + p_2$. It follows that, independently of the presence or absence of the leftover plasma cloud, the pressure inside the molten metal is sufficient to prevent a transition into the gaseous state; bubbles do not appear (i.e., no boiling occurs).

3 Numerical results and discussion

3.1 Results

Let us consider the results obtained by simulations in the framework of the (full) model described above and accounting for all the previously mentioned cathode spot mechanisms, in particular, the effects of the motion of the molten metal and of the plasma production by ionization of vapor emitted in the spot. The temporal evolution of the temperature distribution in the cathode and of the cathode surface deformation is shown in Fig. 2 for the cathode with the microprotrusion and in Fig. 3 for the planar cathode. The temporal evolution of the maximum cathode temperature $T_{\max}$ and of the spot current I is shown in Figs. 4 and 5 by the lines marked by "HD&V".

The temporal evolution in the cases of the cathode with the microprotrusion and of the planar cathode occurs in essentially the same way. At first, the maximum temperature of the cathode rapidly increases; Fig. 4. At 5 ns for the cathode with the microprotrusion and at 8 ns for the planar cathode (Figs. 2a and 3a), $T_{\max}$ has reached a value of approximately $4700 - 4800$ K and changes little from then on until the leftover plasma cloud has been extinguished (at $t = 25$ ns) and the temperature starts falling. In the case of the cathode with the microprotrusion, the protrusion starts melting around 3 ns and is completely destroyed within 14 ns. In both cases, a crater of approximately 1 μm in depth and 5 μm in radius has been formed by the time of extinction of the leftover plasma cloud; Figs. 2b and 3b. An axially symmetric jet develops at the crater periphery (Figs. 2c and

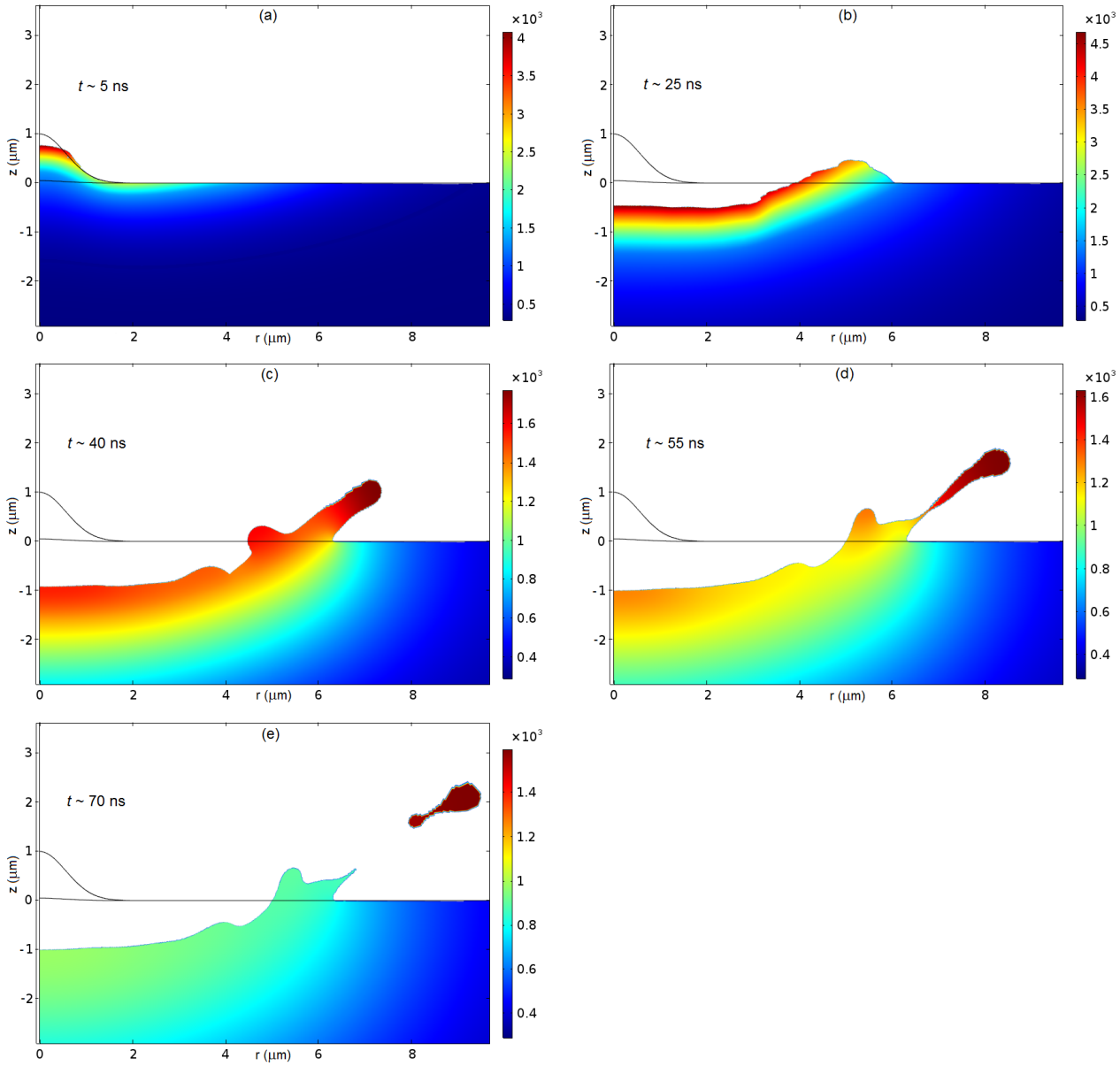

Figure 2. Evolution of the temperature distribution and cathode surface deformation. Cathode with the microprotrusion. The bar in K.

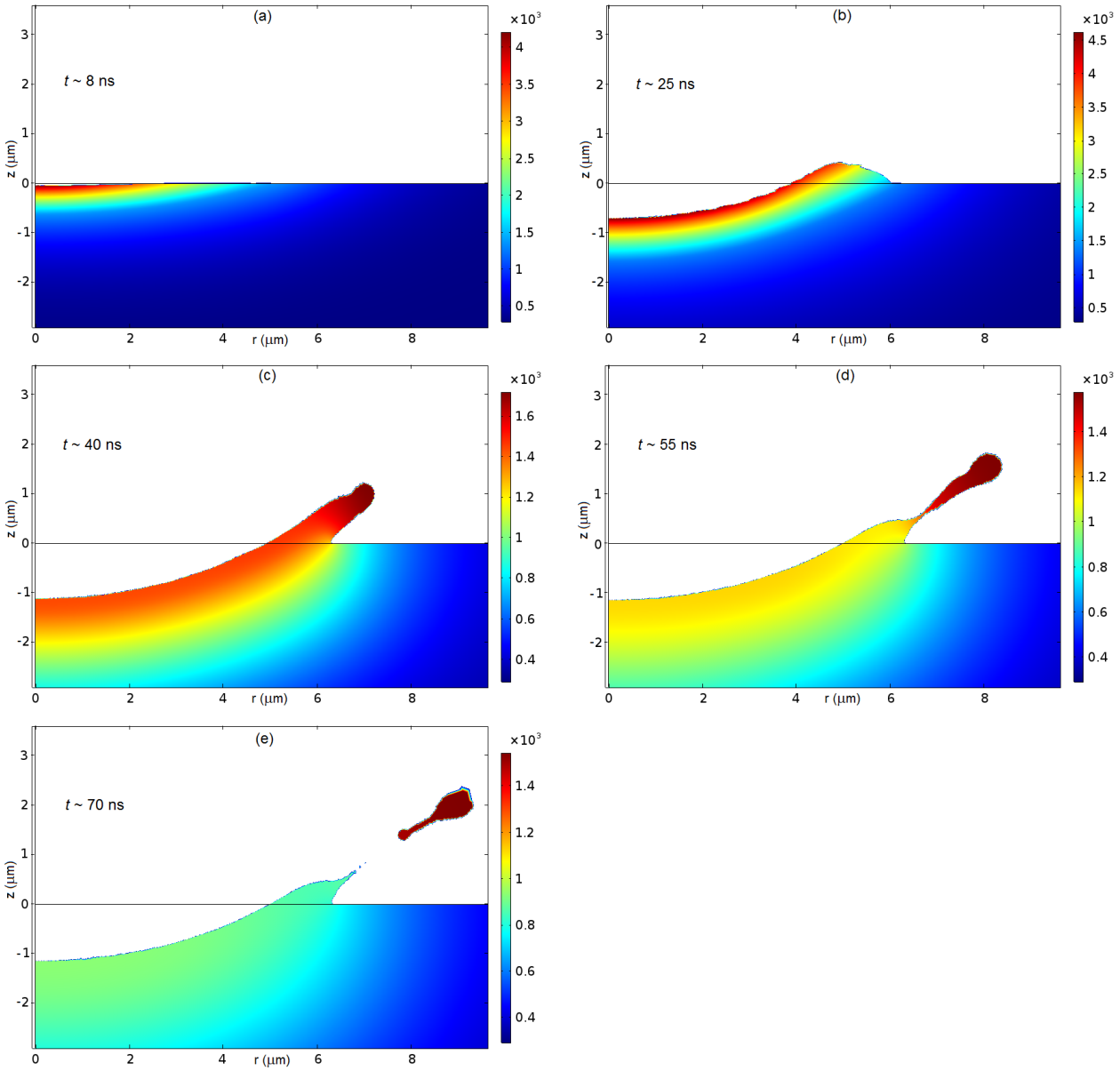

Figure 3. Evolution of the temperature distribution and cathode surface deformation. Planar cathode. The bar in K.

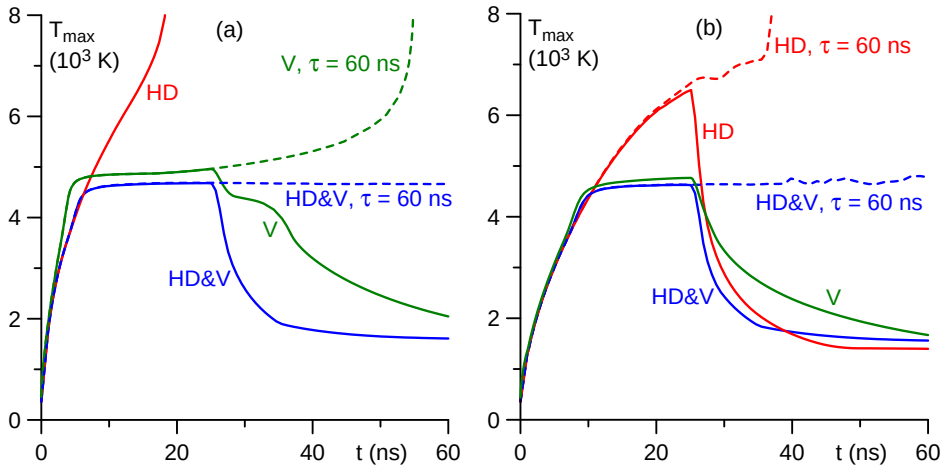

Figure 4. Temporal evolution of the maximum cathode temperature. (a): cathode with the microprotrusion. (b): planar cathode. HD&V: full model. V: model without account of the motion of the melt (the account of the plasma produced in the spot is retained) [7]. HD: model without account of the plasma produced in the spot (the account of the motion of the melt is retained).

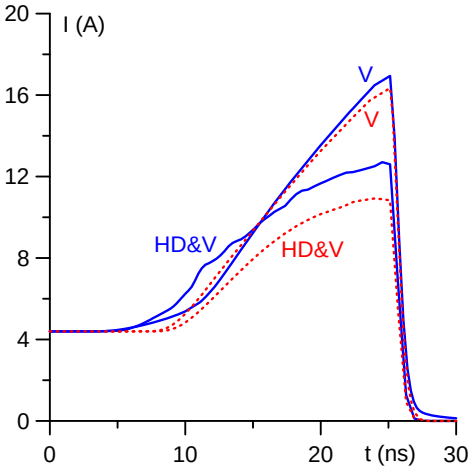

Figure 5. Temporal evolution of the spot current. Solid: cathode with the microprotrusion. Dotted: the planar cathode. HD&V: full model. V: model without account of motion of the molten metal [7].

3c), followed by the detachment of the jet head (Figs. 2d,e and 3d,e). The explosion (thermal runaway) does not occur. Note that the shape of the crater surface in the case of the cathode with the microprotrusion is not smooth, in contrast to the case of the planar cathode, due to the growth of small instabilities that develop as the protrusion is destroyed and are presumably related to the implementation of the level-set method.

Let us now consider the above-described evolution in some detail. The initial phase of the (rapid) temperature increase was interpreted in [7] as the spot ignition phase. The current is constant during this phase as shown by the horizontal section of the dependence $I(t)$ in Fig. 5. Some melting of the cathode surface occurs, however the deformation of the surface on such short times is small; Figs. 2a and 3a. Therefore, the inclusion of the account of the motion of the molten metal in the modeling has not greatly affected the ignition phase and this explains the identical spot ignition times, $t_{ig} \approx 5\,\text{ns}$ for the cathode with the microprotrusion and $t_{ig} \approx 8\,\text{ns}$ for the planar cathode, obtained in this work and in the modeling without account of the motion of the melt [7].

The spot ignition phase is followed by the expansion phase: the spot expands, while the maximum spot temperature changes little. The expansion phase comprises states between (a) and (b) in Figs. 2 and 3. The spot current increases. This is due to the spot expansion and a moderate increase of the current density caused by a weak increase in temperature. The motion of the molten metal comes into play during the expansion phase and the shape of the cathode surface changes and the molten material is pushed outward: a crater with a rim is formed. The main driving mechanism of the motion of the molten metal is the action of the plasma pressure due to incident ions. Craters are thus formed without an explosion, as the maximum temperature of the metal does not exceed $4700 - 4800\,\text{K}$.

The expansion stops at $t = 25\,\text{ns}$, when the leftover plasma cloud is extinguished, and the temperature rapidly decays ($T_{\max} \approx 2000\,\text{K}$ already at $t \approx 30\,\text{ns}$): the spot is quenched by heat removal into the cathode bulk due to thermal conduction. However, the melt velocity is rather high (the maximum velocity is approximately $180\,\text{m/s}$) by the moment when the leftover plasma cloud is extinguished, so a liquid-metal jet is formed under the effect of fluid inertia.

Thus, one can speak of a jet development phase which follows the expansion phase, i.e., starts after the leftover plasma cloud has been extinguished. At $t = 40\,\text{ns}$ (Figs. 2c and 3c), the bottom of the crater has cooled further, the temperature being approximately $1400\,\text{K}$, while the jet head is slightly hotter with a temperature above $1700\,\text{K}$. At $t \approx 55\,\text{ns}$ most of the crater has attained a temperature below the melting temperature of copper, which is $1358\,\text{K}$, and has solidified; Figs. 2d and 3d. The still molten jet head detaches soon after; Figs. 2e and 3e. We remind that the model used in this work is axially symmetric, so the detached droplet is, in fact, a ring. For brevity, we shall continue to refer to the ejected material as a "droplet".

3.2 Effect on the spot development of motion of the melt

Lines "V" in Figs. 4 and 5 depict results of simulation for the same conditions as above-described, but without the account of the motion of the molten metal. (These lines depict data taken from [7]; cf. Figs. 1c and 6a of [7] for the cathode with the micro-

protrusion.) One can see that the evolution of the maximum cathode temperature and spot current with and without account of the melt motion is similar. Moreover, there is little quantitative difference between the values of the maximum cathode temperature for $t \leq 25\,\text{ns}$, i.e., during the ignition and expansion phases; Fig. 4. The value of approximately $4700 - 4800\,\text{K}$ achieved during the expansion phase in both models is the surface temperature at which the combined ion bombardment heating is balanced by the electron emission cooling, as discussed in [7]. Slightly lower values of $T_{\max}$ given by the full model (lines "HD&V" in Figs. 4a and b) result from an additional cooling mechanism in the spot accounted for in this model: the heat transport due to motion of the molten metal.

There is little quantitative difference between the values of the current obtained with and without account of the melt motion during the ignition phase (for $t \leq 5\,\text{ns}$ for the cathode with the microprotrusion and for $t \leq 8\,\text{ns}$ for the planar cathode); Fig. 5. The difference becomes more pronounced during the expansion phase: the maximum current attained with account of the melt motion is of about $10 - 12\,\text{A}$ (lines "HD&V" in Fig. 5), while without the melt motion the current reaches approximately $16\,\text{A}$ (lines "V" in Fig. 5). One of the factors contributing to this difference are the above-mentioned slightly lower values of the surface temperatures and, consequently, of the density of electric current delivered to the cathode by the plasma produced in the spot.

It was shown in [7] that as the Joule heating comes into play in the modeling without account of the motion of the molten metal, the maximum of the cathode temperature is shifted from the surface into the cathode and thermal runaway starts developing. This instability is quenched if the time of action of the leftover plasma cloud is too short; otherwise the explosion occurs. The latter is exemplified by the line marked "V, $\tau = 60\,\text{ns}$" in Fig. 4a for the case of the cathode with the microprotrusion. In this example, the explosion occurs at 55 ns.

In this connection, calculations were also performed with account of the motion of the melt (i.e., by means of the full model) with the time of action of the leftover plasma cloud extended up to 60 ns. The resulting temporal evolution of the maximum cathode temperature is shown in Figs. 4a and 4b by lines marked "HD&V, $\tau = 60\,\text{ns}$". It can be seen that the temperature in the cathode remains limited: thermal runaway does not develop either. Note that the crater continues expanding and the jet does not form.

The spot current and the Joule heating computed with and without the account of the motion of the molten metal with $\tau = 60\,\text{ns}$ are depicted in Fig. 6 by the lines "HD&V, $\tau = 60\,\text{ns}$" and "V, $\tau = 60\,\text{ns}$", respectively. The current computed with the account of the motion of the melt with $\tau = 60\,\text{ns}$ does not change much in the time range $25\,\text{ns} < t < 60\,\text{ns}$ and is around $12\,\text{A}$, while the current computed without the account of the melt motion continues to rapidly increase; Fig. 6a. Therefore, the Joule heating with the account of the melt motion is considerably lower (Fig. 6b), which is why the thermal runaway does not develop.

3.3 Effect of the plasma produced in the spot

The only mechanism of current, momentum, and energy transfer to the cathode surface included in the model of the previous works [5, 6] was the flux of ions from the plasma cloud; the contributions of the vapor emitted in the spot, ions and electrons produced

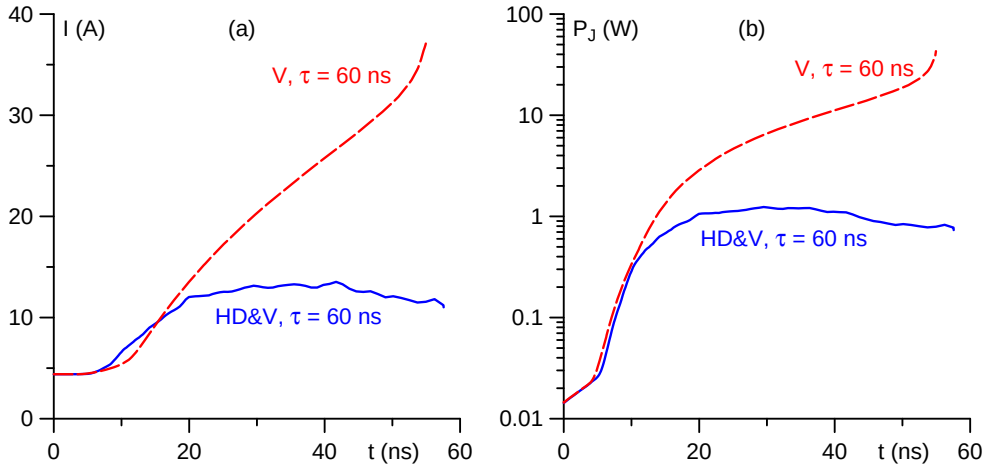

Figure 6. Temporal evolution of the spot current (a) and the power dissipated due to Joule heating (b). Cathode with the microprotrusion. HD&V: full model. V: model without account of motion of the molten metal [7].

by ionization of the vapor, and the electron emission from the cathode surface have been neglected. In designations of this work, the contributions j_2, p_2, and q_2 were taken into account but j_1, p_1, and q_1 neglected. In this section, the effect of the mechanisms represented by the terms j_1, p_1, and q_1 is investigated. For brevity, this effect is referred to as that of the plasma produced in the spot.

Results of simulations performed without account of the terms j_1, p_1, and q_1 are shown by the lines "HD" in Figs. 4a and b. There is no plateau in the evolution of $T_{\max}$, as the cathode surface temperature is not limited by the mechanism of electron emission cooling. In the case of the cathode with the microprotrusion, the critical temperature is reached in $t \approx 19$ ns; line "HD" in Fig. 4a. Note that, in contrast to the case of the model where the plasma produced in the spot is taken into account while the melt motion is neglected [7], the achievement of the critical temperature in these simulations is not due to the development of a thermal instability, but simply due to heating of the cathode surface by an external energy source. In this sense, the term "thermal runaway" does not seem to be appropriate. Another manifestation of the difference between the results of the two models is that $T_{\max}$ in the model without the plasma produced in the spot occurs on the surface, rather than inside the cathode; in this sense, the term "explosion" does not seem to be appropriate either.

The evolution of $T_{\max}$ in the case of the planar cathode (line "HD" in Fig. 4b) is similar but slower: the maximum cathode temperature attained at $t = 25$ ns is approximately 6500 K. If the time of action of the leftover plasma cloud is extended, the critical temperature may be reached at $t \approx 38$ ns; line "HD, $\tau = 60$ ns" in Fig. 4b.

In the case of the cathode with the microprotrusion, the protrusion is destroyed but a crater does not form before the critical temperature has been reached. Heating of the planar cathode is slower, which allows sufficient time for a crater to form. The evolution of the temperature distribution in the planar cathode and of the cathode surface deformation is shown in Fig. 7. The evolution is similar to that found in the framework of the full model and shown in Fig. 3, however, with an important difference: solidification of the

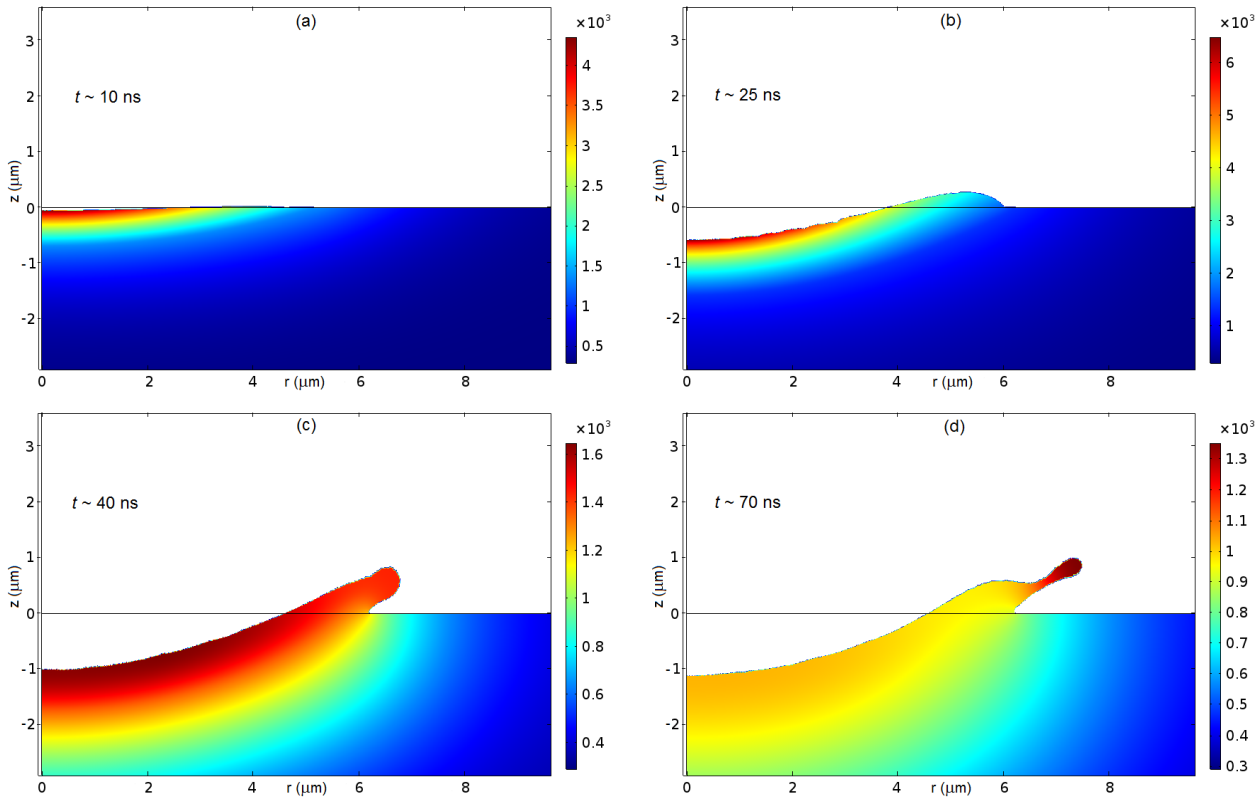

Figure 7. Evolution of the temperature distribution and cathode surface deformation for the case of the planar cathode. The plasma produced by ionization of the emitted vapor is neglected. The bar in K.

liquid metal jet occurred before a droplet could detach; Fig. 7d.

This result can be understood as follows. In the simulations in the framework of the full model, the plasma pressure p_{pl} includes the contribution from the plasma produced in the spot, i.e., $p_{pl} = p_1 + p_2$, and the pressure at the spot center for $t = 25$ ns equals 0.38 GPa. In the modeling where the plasma produced in the spot is neglected, $p_{pl} = p_2$ and the pressure at the spot center for $t \leq 25$ ns equals 0.28 GPa. As a consequence, the maximum force exerted by the plasma pressure p_{pl} on the cathode surface in the full model is about 15% higher as seen in Fig. 8a. The maximum velocity acquired by the molten metal is thus about 40% higher in the framework of the full model (Fig. 8b). For this reason, the speed of motion of the jet under its inertia is greater than the speed of propagation of the solidification front in the jet, culminating in the detachment of the droplet in the framework of the full model. The opposite occurs in the modeling where the plasma produced in the spot is neglected: the speed of propagation of the solidification front, being greater than the speed of the jet head, causes complete solidification before the detachment of the jet head could occur; Fig. 7d. Thus, the pressure exerted by incident ions produced by the ionization of the metal vapor emitted in the spot plays a key role in the detachment of the jet head.

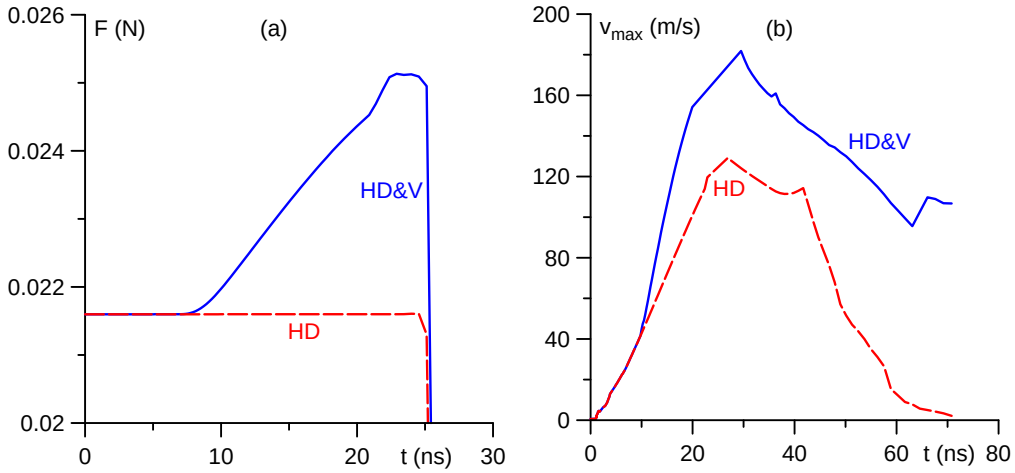

Figure 8. Temporal evolution of the force exerted over the cathode surface by incident ions (plasma pressure) (a) and the maximum velocity acquired by the molten metal (b). Planar cathode.

3.4 Cathode erosion

The modeling results relevant for analysis of cathode erosion are summarized in Table 1. The designations are as follows. $\Gamma_v = \int\int m_i J_v \, dA \, dt$ is the total mass of the vapor emitted from the spot during its lifetime, where J_v is the flux of atoms emitted by the surface estimated by means of the Langmuir formula and the integrals are evaluated over the cathode surface and over the lifetime of the spot. Γ_d is the mass of the ejected droplet. $\Gamma_1 = \Gamma_v - \int\int G \, dA \, dt$ is the mass of the atoms vaporized in the spot that have returned to the cathode surface in the form of ions (here G is the rate of loss of mass by the cathode due to the vaporized atoms that have not immediately returned to the cathode surface; in the framework of the 1D model of near-cathode plasma layers in vacuum arcs [20] employed in this work, G is evaluated as a function of the local cathode surface temperature and near-cathode voltage drop with the use of the self-consistent solution of the Poisson equation describing the space-charge sheath on vaporizing cathodes [21]). $\Gamma_2 = \frac{m_i}{e} j_i^{(\mathrm{cl})} \pi a^2 \tau$ is the total mass of the ions from the leftover plasma cloud that have reached the cathode surface during the lifetime of the spot. $Q_1 = \int\int j_1 \, dA \, dt$ and $Q_2 = j_i^{(\mathrm{cl})} \pi a^2 \tau$ are charges transported to the cathode by the plasma produced in the spot (including the emission current) and by the ions from the plasma cloud, respectively. Finally, $\gamma_v = (\Gamma_v - \Gamma_1)/\Gamma_v$ is the fraction of the vaporized atoms that have not immediately returned to the cathode surface; the so-called escape factor.

The rate of erosion of electrodes is usually characterized by the specific erosion (the so-called g-factor), defined as the loss of mass by the electrode per unit charge transported. In this connection, also shown in Table 1 are quantities $g_\alpha = \Gamma_\alpha / Q$, $\alpha = 2, v, d$, where $Q = Q_1 + Q_2$ is the total charge transported in the spot.

Before discussing the data shown in Table 1, it is convenient to give a few simple considerations based on available experimental information. If there are no explosions that could result in the emission of ionized cathode material or solid particles, then the transport of mass from the cathode into the near-cathode plasma is due to the emission

	microprotrusion	planar
$\Gamma_v\,(10^{-12}\,\mathrm{g})$	6	5
$\Gamma_d\,(10^{-12}\,\mathrm{g})$	210	220
$\Gamma_1\,(10^{-12}\,\mathrm{g})$	5.2	4.3
$\Gamma_2\,(10^{-12}\,\mathrm{g})$	74	74
$Q_1\,(\mu\mathrm{C})$	0.1	0.07
$Q_2\,(\mu\mathrm{C})$	0.11	0.11
γ_v	0.13	0.14
$g_2\,(\mu\mathrm{g/\,C})$	340	400
$g_v\,(\mu\mathrm{g/\,C})$	28	27
$g_d\,(\mu\mathrm{g/\,C})$	980	1200

Table 1. Relevant erosion data computed in the framework of the model of this work.

of vapor and the ejection of droplets: $\Gamma_+ = \Gamma_v + \Gamma_d$. The material returns to the cathode surface in the form of ions: $\Gamma_- = \Gamma_1 + \Gamma_2$. The net loss of mass of the cathode caused by the existence of an individual spot is

$$\Gamma = \Gamma_v + \Gamma_d - \Gamma_1 - \Gamma_2. \tag{15}$$

Dividing Eq. (15) by Q, one can write it in the form

$$g = \gamma_v g_v + g_d - g_2, \tag{16}$$

where $g = \Gamma/Q$ is the specific erosion of the cathode.

Since $\Gamma_2 = m_i Q_2/e$, one can write

$$g_2 = \frac{Q_2 m_i}{e\,(Q_1 + Q_2)}. \tag{17}$$

An upper estimate of the rhs can be obtained by neglecting the charge transport by the plasma produced in the spot, following [5]. A bit more realistic estimate can be obtained by assuming that contributions of the cloud and the plasma produced in the spot (once again, including the emission current) are comparable. Setting in Eq. (17) $Q_1 = Q_2$, one obtains $g_2 = 330\,\mu\mathrm{g/\,C}$.

Assuming that most of the vaporized atoms are ionized in the immediate vicinity of the cathode surface and return to the cathode surface as ions, one can drop the first term on the rhs of Eq. (16). Experimental values $g = 115 - 130\,\mu\mathrm{g/\,C}$ have been reported for the erosion for copper cathodes [29]. Setting in Eq. (16) $g = 120\,\mu\mathrm{g/\,C}$, one can estimate the specific mass flux from the cathode surface related to the droplet ejection: $g_d = 450\,\mu\mathrm{g/\,C}$.

The droplets are partially vaporized in the very dense and hot plasma ball adjacent to the spot; e.g., [30]. The vapor is ionized and a part of the produced ions move away from the cathode with the plasma jet. The rest of the ions remain in the near-cathode region and thus form a new plasma cloud, which will eventually ignite the next spot. The flux of the ions in the vacuum arc plasma jet (the so-called ion erosion) measured for copper

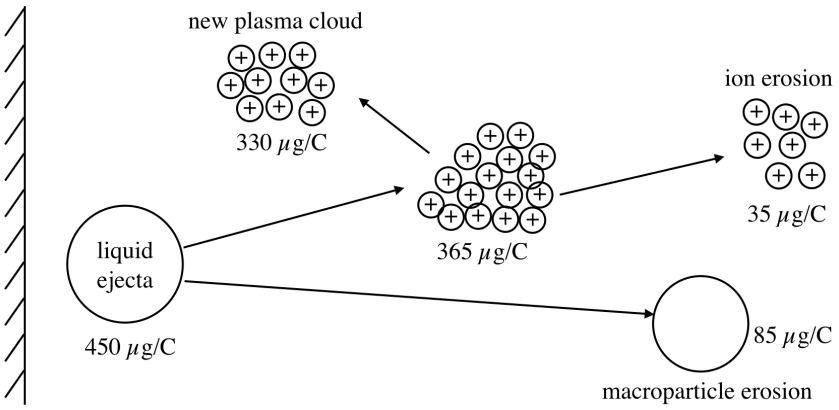

Figure 9. Schematic of cathode erosion.

cathodes is $33-37\,\mu g/\,C$ [31, p. 157], hence the flux of the liquid phase may be estimated as $120\,\mu g/\,C - 35\,\mu g/\,C = 85\,\mu g/\,C$. It follows that of the initial mass of the droplet ejected only about $85\,\mu g/\,C$ move into the bulk of the arc in the form of a droplet. The rest of the mass of the droplet, $365\,\mu g/\,C$, is vaporized in the plasma ball, with $330\,\mu g/\,C$ forming the new plasma cloud in the near-cathode region and $35\,\mu g/\,C$ going into the bulk with the jet in the form of ions. A schematic illustrating these estimates is shown in Fig. 9.

The above estimates are based on experimental values. They do not make use of results of simulations of this work and can therefore be compared with these results. In fact, the results shown in Table 1 conform to the estimates. Values of Q_1 and Q_2 in Table 1 are indeed comparable as assumed above. It is not surprising therefore that the values of g_2 the specific mass flux from the plasma cloud in Table 1 are close to the estimated value of $330\,\mu g/\,C$. The specific flux of ions originating in the vaporization of the cathode surface which do not return to the cathode, $\gamma_v g_v$, evaluated using γ_v and g_v from Table 1, amounts to about $3.7\,\mu g/\,C$ and is much smaller than the other terms of Eq. (16) as expected.

As previously discussed, the assumption of axial symmetry in the modeling leads to the formation of an axially symmetric jet at the crater periphery and the detachment of a ring. In reality, however, neither the leftover plasma cloud that causes spot ignition nor protrusions on the surface of the cathode are axially symmetric, thus a ring jet cannot develop; instead, one or a few 3D jets will be formed. Another reason for breaking of the axial symmetry may be the development of the Rayleigh-Plateau hydrodynamic instability at the crater rim [5, 32–34]. Thus, the mass of the computed hypothetical ring gives an upper estimate of the mass of the ejected droplet. Indeed, the values of g_d of $980\,\mu g/\,C$ and $1200\,\mu g/\,C$ appearing in Table 1, exceed the value of $450\,\mu g/\,C$ deduced above from the experimental data by a factor of 2.2 or 2.7. In other words, no more than approximately 40% of the material constituting the hypothetical ring computed in the axially symmetric geometry actually detaches from the surface.

It is of interest to estimate the energy deposited in the plasma ball by the plasma produced in the spot during its lifetime. This energy may be estimated as $\int\int \frac{j_1}{e} 3.2kT_e^{(1)}\,dA\,dt$

(here $T_e^{(1)}$ is the temperature of electrons in the near-cathode layer, which is computed as a function of the local cathode surface temperature and near-cathode voltage drop by means of the code [20]) and equals $1.5\,\mu$J for the cathode with the microprotrusion and $1.1\,\mu$J for the planar cathode. In order for the model to be self-consistent, this energy should coincide with, or exceed, the energy needed to vaporize and ionize a part of the ejected droplet and thus form a new plasma cloud similar to the original leftover plasma cloud assumed in the modeling to ignite the spot. The latter energy cannot be computed without accurate 3D simulations of the detachment of the droplets, their interaction with the near-cathode plasma, and vaporization. However, one can perform a crude estimate with the use of the above-given simple considerations based on available experimental information: $365\frac{\mu g}{C}\frac{0.2\,\mu C}{m_i}\left(A_v + A_i + \frac{3}{2}kT_e\right) = 1.5\,\mu$J. This value coincides with the above value of the deposited energy in the case of the cathode with the microprotrusion. There is an energy deficit in the case of the planar cathode, however this deficit is modest and certainly below the margin of error of the estimates.

3.5 Comparison with other cathode spot models

Various modes of the crater formation process have been identified in the modeling [5]. If the maximum pressure exerted over the cathode by the plasma cloud was set equal to $0.1 - 0.2\,$GPa (this pressure was treated in [5] as an input parameter), then the inertial splashing mode occurred: the velocity acquired by the molten metal during the time of action of the leftover plasma cloud leads to the formation of a jet after the cloud has been extinguished. The active splashing mode occurred at a pressure of $0.4\,$GPa: the jet has developed and the critical temperature is reached during the time of action of the cloud.

In the modeling of this work, the jet formation occurs due to inertia, as in the inertial splashing mode of [5]. However, the computed plasma pressure attains a maximum value of approximately $0.38\,$GPa, which is comparable with that required for the active splashing mode in [5]. Other substantial differences are that the detachment of a droplet was not observed in the modeling [5], while in the modeling of this work the heating up to the critical temperature was not observed.

The different results obtained in [5] and in this work are owed to the neglect of the interaction of the plasma produced in the spot with the cathode surface in the model [5], in particular the neglect of the cooling due to electron emission and of the pressure exerted by the ions produced from the metal vapor emitted in the spot. The former limits the cathode temperature, while the latter provides the necessary acceleration to the molten metal so that a droplet may detach from the jet before the solidification front has reached the jet head.

The modeling of this work could have, in principle, confirmed the physical picture of the ecton concept described in Sec. 1, since all relevant mechanisms are taken into account. However, no explosions are observed in the conditions considered in this work; there is no appreciable effect of the pre-existing μm-size protrusion; craters are formed and droplets detach without an explosion; and even without an explosion, the ejected material and the energy deposited in the plasma are sufficient to instigate the formation of a new plasma cloud that will ignite a subsequent spot.

Another physical picture of cathode spot development was proposed in [35, 36]: an

external plasma heats the cathode and initiates the spot; once the external plasma has been extinguished, the spot evolves until a steady state is reached. The results of the modeling of this work are in a clear contradiction with the latter conclusion. The model [35, 36] differs from the model of this work in a number of important aspects: the heat conduction in the cathode is treated by means of an equation of integral heat balance instead of the differential equation (which results in a loss of information and, consequently, the model not being self-consistent [37]); the development of a spot is computed for a given value of the spot current (and not of the near-cathode voltage drop, as done in this work in order to simulate high-current vacuum arcs); and the hydrodynamic phenomena are not taken into account. Presumably, the latter difference is the most important one: the account of motion of the molten metal, taken into account in this work, prevents a spot from attaining a steady state.

4 Summary and concluding remarks

The developed model describes the initiation and development of an individual cathode spot in a high-current vacuum arc with account of the most important mechanisms: the bombardment of the cathode surface by ions coming from a previously existing plasma; vaporization of the cathode material in the spot, its subsequent ionization and the interaction of the produced plasma with the cathode; Joule heating in the cathode body; motion of the molten metal under the effect of pressure exerted by the plasma and the Lorentz force and related phenomena.

The results of the modeling allow one to identify three phases of the spot life cycle. The ignition phase is characterized by a rapid increase of the cathode temperature up to $4700 - 4800\,\mathrm{K}$ and lasts for approximately 5 ns on the cathode with the microprotrusion and 8 ns on the planar cathode; Figs. 2a and 3a. Some melting of the cathode surface occurs, however the deformation of the surface on such short times is small. Therefore, the spot development during this phase occurs essentially in the same way as in the modeling without account of the motion of the melt [7].

The subsequent expansion phase is characterized by a plateau in the temporal evolution of $T_{\max}$ and an increase in the spot current I. A crater is formed due to the displacement of the molten metal from the center of the spot due to the pressure exerted by the plasma.

After the leftover plasma cloud has been extinguished at $t = 25\,\mathrm{ns}$ (Figs. 2b and 3b), no more energy is supplied to the cathode. The crater expansion stops and the spot starts being rapidly destroyed by heat removal into the bulk of the cathode due to thermal conduction. However, the melt velocity is quite high at this moment, leading to the formation of a liquid-metal jet under the effect of fluid inertia; Figs. 2c and 3c. This stage may be called the jet development phase. It culminates in the detachment of the head of the jet: a droplet appears; Figs. 2d, e and 3d, e.

The cathode temperature does not exceed $4700 - 4800\,\mathrm{K}$ during the whole lifetime of the spot even if the time of action of the plasma cloud is extended. This is a consequence of the cooling due to electron emission and of convective heat transfer. If the latter mechanism is discarded, then the Joule heating becomes sufficient to initiate the thermal

runaway inside the cathode body and the temperature reaches the critical temperature of copper: a microexplosion occurs; e.g., line "V, $\tau = 60\,\mathrm{ns}$" in Fig. 4a. In the simulations where the contribution of the plasma produced in the spot (and the electron emission cooling) is discarded, the critical temperature is attained as well; e.g., line "HD" in Fig. 4a. However, the temperature maximum occurs on the cathode surface in this case; the achievement of the critical temperature is simply due to heating by an external source rather than due to the development of a thermal instability (thermal runaway). In this sense, the term "explosion" is not appropriate in this case.

Craters are formed during the expansion phase, under the action of the pressure exerted by the plasma over the cathode surface. Jet formation and droplet detachment occur under the effect of fluid inertia once the leftover plasma cloud has been extinguished. Thus, craters form and droplets detach without an explosion. Moreover, the spot and cathode surface evolution are essentially the same on both the planar cathode and the cathode with the $1\,\mu$m-scale microprotrusion: the presence of a surface nonuniformity has no appreciable effect on the spot development.

The pressure exerted over the cathode by the ions produced from the metal vapor emitted in the spot is significantly higher than the saturated vapor pressure. It follows that, independently of the presence or absence of the leftover plasma cloud, the pressure inside the molten metal is sufficient to prevent a transition into the gaseous state; bubbles do not appear and no boiling occurs.

The modeling results conform to estimates of different mechanisms of cathode erosion, derived from experimental data on the net and ion erosion of copper cathodes of vacuum arcs. The loss of mass of the cathode due to vaporization is virtually compensated by the return of the vaporized atoms in the form of ions, so the dominant erosion mechanism is the ejection of liquid droplets, partially compensated by ion flux from the plasma cloud. The emitted droplets are partially vaporized in the near-cathode region. The produced vapor is ionized and a part of the ions move away from the cathode with the plasma jet. The rest of the ions remain in the near-cathode region and thus form a new plasma cloud, which will eventually ignite the next spot.

In real experimental situations, neither the leftover plasma cloud nor protrusions on the surface of the cathode are axially symmetric, hence the droplets are 3D rather than ring-shaped, as in the (axially symmetric) modeling of this work. Thus, the computed mass of the hypothetical ejected ring gives only an upper estimate of the mass of the ejected droplet: the former exceeds the latter by a factor of about 2.5.

One can hope that the model of this work can be used, with appropriate modifications, for investigation of plasma-electrode interaction and crater formation in discharges of other types, for instance, ignition discharges in spark plugs (e.g., [38–40] and references therein) and discharges between electrodes in liquids (e.g., [41, 42] and references therein).

Acknowledgments The work at Universidade da Madeira was partly supported by FCT - Fundação para a Ciência e a Tecnologia of Portugal (the project Pest-OE/UID/FIS/50010/2
and by Siemens AG.

The authors are thankful to K. G. Honnell and S. D. Crockett of Group T-1 of the Los Alamos National Laboratory for providing the equation of state data for copper from the SESAME EOS library. One of the authors (MSB) appreciates many stimulating discussions with S. M. Shkol'nik.

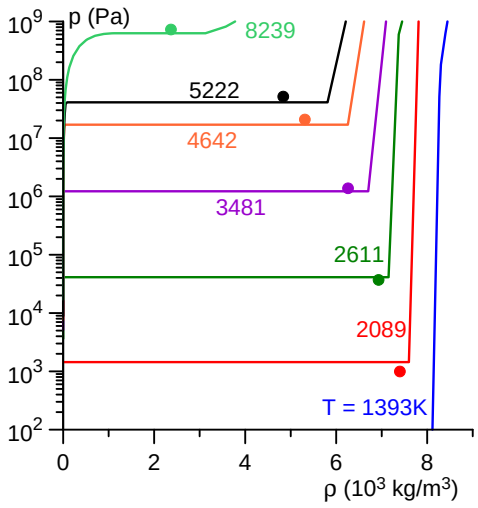

Figure 10. Lines: data on the equation of state for copper [50]. Points: mass density of liquid copper evaluated by means of a fit formula with the use of data [18, 52] and saturated vapor pressure evaluated by means of the formula [53].

After the completion of this work, one of the authors and the initiator of the work passed away prematurely. His coworkers dedicate this paper to the glowing memory of Werner Hartmann, a brilliant scientist and a dear friend.

A Equation of state

The microexplosion scenario on the cathode of a vacuum arc has a number of features in common with the electrical explosion of wires. A routine approach to modeling of the wire explosion is based on the use of 1D magnetohydrodynamic simulations with an equation of state (EOS) of the metal for a wide range of temperatures and pressures; e.g., [43–46]. Similar wide-range EOS are used in the models of vacuum arc-cathode interaction assuming a continuous metal-plasma transition without an interface [47–49]. The approach to the modeling of cathode spots employed in this work does not assume a continuous metal-plasma transition nor do the modeling results reveal microexplosions, but the question as to whether a wide-range EOS should be implemented is still relevant.

Lines in Fig. 10 represent isotherms of copper given by the wide-range EOS of copper [50] for several temperature values below the critical temperature (8390 K). The data were provided by the Group T-1 at the Los Alamos National Laboratory with the use of the SESAME EOS Library [51] maintained by the group. Three branches are identifiable: the gas state branch at low mass densities, which coincides with the ordinate axis; the liquid state branch at high mass densities; and the vapor-liquid equilibrium branch at intermediate mass densities (the liquid and gas phases coexist at equilibrium and variations of volume occur at a constant pressure).

The simulations of this work reveal that the maximum temperature $T_{\max}$ in the cathode is limited to approximately $4700-4800$ K. One can see in Fig. 10 that in this temperature range and in the relevant pressure range (up to 1 GPa; cf. Fig. 1) the dependence of the

mass density of liquid copper on pressure is weak. The dependence on temperature is more appreciable, although not very significant: ρ decreases from $8000\,\mathrm{kg/\,m^3}$ at low temperatures to approximately $6000\,\mathrm{kg/\,m^3}$ at high temperatures.

Thus, an accurate equation of state for a wide range of temperatures and pressures is not critical for the modeling of cathode spots performed in this work: it is sufficient to take into account the variation of the mass density of liquid copper with temperature. In this work, the function $\rho\,(T)$ was evaluated with the use of data from [18, 52, 54] as in [7].

It is of interest to compare values given by the above-mentioned function $\rho\,(T)$ with the data given by the wide-range EOS of copper [50] and shown in Fig. 10. Furthermore, it is appropriate to also compare the latter data with those given by the formula [53] for the saturated vapor pressure of copper, used in the model of near-cathode plasma layers in vacuum arcs developed in [20] and employed in this work. This comparison is illustrated by the points in Fig. 10: the abscissas of these points represent values of the function $\rho\,(T)$ and the ordinates represent the saturated vapor pressure evaluated by means of the formula [53]. (Note that the vapor pressure of copper given by the formula [53] for $T = 8390\,\mathrm{K}$, $0.79\,\mathrm{GPa}$, is close to the pressure at the critical point of copper given in [54], which is $0.75\,\mathrm{GPa}$.) One can see that the data used in this work do not deviate greatly from the EOS data [50].

References

[1] B. Jüttner, J. Phys. D: Appl. Phys. **34**, R103 (2001).

[2] G. A. Mesyats and S. A. Barengol'ts, Physics - Uspekhi **45**, 1001 (2002).

[3] G. A. Mesyats, Plasma Phys. Control. Fusion **47**, A109 (2005).

[4] R. Schmoll, J. Phys. D: Appl. Phys. **31**, 1841 (1998).

[5] G. A. Mesyats and I. V. Uimanov, IEEE Trans. Plasma Sci. **43**, 2241 (2015).

[6] G. A. Mesyats and I. V. Uimanov, IEEE Trans. Plasma Sci. **45**, 2087 (2017).

[7] M. D. Cunha, H. T. C. Kaufmann, M. S. Benilov, W. Hartmann, and N. Wenzel, IEEE Trans. Plasma Sci. **45**, 2060 (2017).

[8] V. R. Voller and C. Prakash, Int. J. Heat Mass Transfer **30**, 1709 (1987).

[9] A. D. Brent, V. R. Voller, and K. J. Reid, Numerical Heat Transfer **13**, 297 (1988).

[10] R. W. Lewis and K. Ravindran, Int. J. Numer. Meth. Engng. **47**, 29 (2000).

[11] E. Olsson and G. Kreiss, J. Comput. Phys. **210**, 225 (2005).

[12] E. Olsson, G. Kreiss, and S. Zahedi, J. Comput. Phys. **225**, 785 (2007).

[13] J. U. Brackbill, D. B. Kothe, and C. Zemach, J. Comput. Phys. **100**, 335 (1992).

[14] L. Wang, S. Jia, D. Yang, K. Liu, G. Su, and Z. Shi, J. Phys. D: Appl. Phys. **42**, 145203 (2009).

[15] L. Wang, S. Jia, Y. Lin, B. Chen, D. Yang, and Z. Shi, J. Appl. Phys. **107**, 113306 (2010).

[16] L. Wang, X. Zhou, H. Wang, Z. Qian, S. Jia, D. Yang, and Z. Shi, IEEE Trans. Plasma Sci. **40**, 2237 (2012).

[17] X. Huang, L. Wang, J. Deng, S. Jia, K. Qin, and Z. Shi, J. Phys. D: Appl. Phys. **49**, 075202 (2016).

[18] M. J. Assael, A. E. Kalyva, K. D. Antoniadis, R. M. Banish, I. Egry, J. Wu, E. Kaschnitz, and W. A. Wakeham, J. Phys. Chem. Ref. Data **39**, 033105 (2010).

[19] T. Matsumoto, H. Fujii, T. Ueda, M. Kamai, and K. Nogi, Measurement Science and Technology **16**, 432 (2005).

[20] N. A. Almeida, M. S. Benilov, L. G. Benilova, W. Hartmann, and N. Wenzel, IEEE Trans. Plasma Sci. **41**, 1938 (2013).

[21] M. S. Benilov and L. G. Benilova, J. Phys. D: Appl. Phys. **43**, 345204 (12pp) (2010).

[22] E. L. Murphy and R. H. Good, Phys. Rev. **102**, 1464 (1956).

[23] E. Hantzsche, IEEE Trans. Plasma Sci. **17** (1989), 10.1109/27.41176.

[24] I. G. Brown and X. Godechot, IEEE Trans. Plasma Sci. **19**, 713 (1991).

[25] V. F. Puchkarev and A. M. Murzakayev, J. Phys. D: Appl. Phys. **23**, 26 (1990).

[26] G. A. Mesyats, IEEE Trans. Plasma Sci. **23**, 879 (1995).

[27] G. A. Mesyats, IEEE Trans. Plasma Sci. **41**, 676 (2013).

[28] A. Anders, S. Anders, B. Juettner, and H. Lueck, IEEE Trans. Plasma Sci. **24**, 69 (1996).

[29] B. Juettner and V. Puchkarev, in *Handbook of Vacuum Arc Science and Technology: Fundamentals and Applications*, edited by R. L. Boxman, D. M. Sanders, and P. J. Martin (Noyes Publications, Park Ridge, N.J., U.S.A., 1995) pp. 73–151.

[30] E. Hantzsche, in *Handbook of Vacuum Arc Science and Technology: Fundamentals and Applications*, edited by R. L. Boxman, D. M. Sanders, and P. J. Martin (Noyes Publications, Park Ridge, N.J., U.S.A., 1995) pp. 151–208.

[31] A. Anders, *Cathodic Arcs: From Fractal Spots to Energetic Condensation*, Springer Series on Atomic, Optical, and Plasma Physics (Springer, New York, 2008).

[32] G. A. Mesyats and N. M. Zubarev, J. Appl. Phys. **117**, 043302 (2015).

[33] M. A. Gashkov, N. M. Zubarev, O. V. Zubareva, G. A. Mesyats, and I. V. Uimanov, J. Exp. Theor. Phys. **122**, 776 (2016).

[34] M. A. Gashkov, N. M. Zubarev, G. A. Mesyats, and I. V. Uimanov, Tech. Phys. Lett. **42**, 852 (2016).

[35] I. I. Beilis, Appl. Phys. Lett. **97**, 121501 (2010).

[36] I. I. Beilis, IEEE Trans. Plasma Sci. **41**, 1979 (2013).

[37] M. S. Benilov, IEEE Trans. Plasma Sci. **32**, 249 (2004).

[38] F. A. Soldera, F. T. Mucklich, K. Hrastnik, and T. Kaiser, IEEE Trans. Vehicular Tech. **53**, 1257 (2004).

[39] N. Jeanvoine and F. Muecklich, J. Phys. D: Appl. Phys. **42**, 035203 (2009).

[40] N. Jeanvoine, *Plasma-material interaction and electrode degradation in high voltage ignition discharges*, Ph.D. thesis, Universitaet des Saarlandes, Saarbruecken (2009).

[41] A. Hamdan, C. Noel, F. Kosior, G. Henrion, and T. Belmonte, J. Appl. Phys. **113**, 043301 (2013).

[42] A. Hamdan, F. Kosior, C. Noel, G. Henrion, J. N. Audinot, T. Gries, and T. Belmonte, J. Appl. Phys. **113**, 213303 (2013).

[43] S. I. Tkachenko, K. V. Khishchenko, V. S. Vorob'ev, P. R. Levashov, I. V. Lomonosov, and V. E. Fortov, High Temp. **39**, 674 (2001).

[44] V. I. Oreshkin, S. A. Barengol'ts, and S. A. Chaikovsky, Tech. Phys. **52**, 642 (2007).

[45] D. Sheftman and Y. E. Krasik, Phys. Plasmas **17**, 112702 (2010).

[46] A. E. Barysevich and S. L. Cherkas, Phys. Plasmas **18**, 052703 (2011).

[47] H. Hess, J Phys. D: Appl. Phys. **24**, 36 (1991).

[48] D. L. Shmelev and E. A. Litvinov, IEEE Trans. Plasma Sci. **25**, 533 (1997).

[49] D. L. Shmelev and E. A. Litvinov, IEEE Trans. Dielectrics Elect. Insulation **6**, 441 (1999).

[50] J. H. Peterson, K. G. Honnell, C. W. Greeff, J. D. Johnson, J. C. Boettger, and S. D. Crockett, in *American Institute of Physics Conference Series*, Vol. 1426 (2012) pp. 763–766.

[51] S. P. Lyon and J. D. Johnson, *SESAME: The Los Alamos National Laboratory Equation of State Database*, Tech. Rep. (Los Alamos National Laboratory, 1992).

[52] J. A. Cahill and A. D. Kirshenbaum, J. Phys. Chem. **66**, 1080 (1962).

[53] D. R. Lide, ed., *CRC Handbook of Chemistry and Physics*, 84th ed. (CRC Press, Boca Raton, 2003-2004).

[54] V. E. Fortov, I. T. Iakubov, and A. G. Khrapak, *Physics of Strongly Coupled Plasma* (Oxford University Press, Oxford, 2007).